

## CORES AND CUSPS IN WARM DARK MATTER HALOS

FRANCISCO VILLAESCUSA-NAVARRO  
Instituto de Física Corpuscular (IFIC), E-46071, Valencia, Spain

NEAL DALAL

Canadian Institute for Theoretical Astrophysics, Univ. of Toronto, 60 St. George St., Toronto, ON, M5S3H8, Canada  
*Draft version October 19, 2018*

### ABSTRACT

The apparent presence of large core radii in Low Surface Brightness galaxies has been claimed as evidence in favor of warm dark matter. Here we show that WDM halos do not have cores that are large fractions of the halo size: typically,  $r_{\text{core}}/r_{200} \lesssim 10^{-3}$ . This suggests an astrophysical origin for the large cores observed in these galaxies, as has been argued by other authors.

### 1. INTRODUCTION

The highly successful cold dark matter (CDM) model idealizes the thermal motions of dark matter particles as negligible on all scales at high redshift. In this model, perturbation modes on all scales are gravitationally unstable, leading to hierarchical structure formation in which nonlinear structures such as halos assemble through numerous mergers. Numerical simulations of structure formation within CDM models indicate that halos are predicted to have steep central density profiles, with logarithmic slopes  $d \log \rho / d \log r \sim -1$  on the smallest resolved scales (see Navarro et al. (2010) for a recent example).

In many DM models, however, the DM temperature is nonzero, which can affect the properties of DM halos in multiple ways. For example, a finite DM temperature suppresses the abundance of low-mass halos. This occurs because, following freezeout of dark matter interactions, DM particles freely stream over some distance determined by their thermal velocities, and density fluctuations on scales below this free-streaming scale  $r_{\text{fs}}$  are highly suppressed. Roughly speaking, the smallest halos that arise are expected to have masses of order  $M_{\text{fs}} = (4\pi/3)\bar{\rho}_m r_{\text{fs}}^3$ , although N-body simulations have not definitively ruled out the formation of at least some halos below  $M_{\text{fs}}$  through non-hierarchical processes like fragmentation (Wang & White 2007).

Besides this suppression of the abundance of halos, a nonzero DM temperature also can affect the central density profiles of the halos that do form. One elegant way to see this is to note that the DM phase space density is finite if the DM temperature is finite, and since DM is taken to be collisionless, then Liouville's theorem guarantees that the phase space density cannot increase. Hence, the phase space density is bounded within DM halos (Tremaine & Gunn 1979), which implies that the central slope of the DM density profile must vanish (e.g. Tremaine et al. 1994). In other words, halos are expected to have central cores if the DM is not cold. Note that this effect is caused by the finite DM temperature at the time of formation of the halo, and is not due to the truncation of the small-scale linear power spectrum (Wang & White 2009).

Therefore, increasing the DM temperature has the ef-

fect of suppressing the number of low-mass halos, and of producing central cores in DM halos. Observationally, there may be evidence for both of these effects. The observed number of Local Group satellite galaxies falls well below the thousands of DM subhalos found in CDM simulations of halos like our Galaxy's (see Kravtsov (2010) for a recent review). In addition, the 21 cm rotation curves of certain galaxies, in particular low surface brightness (LSB) galaxies, appear better fit by cored DM profiles than cuspy DM profiles (see Kuzio de Naray et al. (2010) for a recent discussion). For these reasons, there has been considerable interest in the literature in investigating structure formation in models where DM is not perfectly cold. In so-called Warm Dark Matter (WDM) models, the DM temperature is chosen to make the free-streaming scale correspond to subgalactic scales,  $r_{\text{fs}} \sim 0.1 h^{-1} \text{Mpc}$  (Bode et al. 2001).

WDM models have become increasingly disfavored in recent years, in large part because of constraints on the matter power spectrum derived from the Lyman- $\alpha$  forest flux power spectrum (Seljak et al. 2006). The observational support for WDM models from dwarfs and LSB galaxies has also eroded, as faint Local Group satellites have been discovered in increasing numbers (e.g. Belokurov et al. 2007; Tollerud et al. 2008; Kravtsov 2010) thanks to the Sloan Digital Sky Survey. Recently, Kuzio de Naray et al. (2010) have argued that the large cores apparently observed in certain LSB galaxies cannot all be due to WDM, since the implied central phase space densities in these systems are not universal, but instead show large variations from object to object. This suggests an astrophysical origin for claimed detections of central cores, and mechanisms to produce such cores have been proposed (e.g. Governato et al. 2009).

In this paper, we present yet another argument against WDM as the origin of large cores in halo density profiles. As discussed by Kuzio de Naray et al. (2010), the inferred core radii in several LSB galaxies are large fractions of the halo virial radii,  $r_{\text{core}} \sim 5\% r_{200}$ . As mentioned above, such large cores do not arise in CDM models, and so we might naturally consider producing large cores by raising the DM temperature. Making the DM warm, however, has the side effect of wiping out small halos, and so it is not obvious that raising the DM temperature can gener-

ate halos with large  $r_{\text{core}}/r_{200}$ .

We can, however, use a simple argument to make an order-of-magnitude estimate of this ratio. Consider a WDM particle of mass  $m$  and typical momentum  $p$ . Following freezeout, its momentum redshifts as  $p \propto a^{-1}$ , so let us write  $p = mv_0/a$ , where  $v_0$  is the velocity today at  $z = 0$  (since WDM must be nonrelativistic today,  $v_0 \ll 1$ ). The particle's velocity is then  $v(a) = v_0/\sqrt{v_0^2 + a^2}$  (using units where  $c = 1$ ). Neglecting accelerations caused by gravitational potential fluctuations, the particle freely streams a comoving distance

$$r_{\text{fs}} = \int \frac{v dt}{a} \sim \frac{v_0}{\Omega_r^{1/2} H_0} \log\left(\frac{a_{\text{eq}}}{v_0}\right), \quad (1)$$

where we assume  $v_0 \ll a_{\text{eq}} = \Omega_r/\Omega_m$ . This distance encloses mass  $M_{\text{fs}} = (4\pi/3)\bar{\rho}_m r_{\text{fs}}^3$ , and as noted above, the smallest halos that form will have masses of order  $M_{\text{fs}}$ . The virial velocities of these halos at their formation epoch  $a_c$  are

$$v_{200} = \left(\frac{GM_{\text{fs}}}{r_{200}}\right)^{1/2} = \left(\frac{\Omega_m \Delta_{200}^{1/3}}{2a_c}\right)^{1/2} H_0 r_{\text{fs}}, \quad (2)$$

where  $\Delta_{200} \approx 200$  is the virial overdensity. Now, because the thermal velocity  $v_{\text{th}} \approx v_0/a_c$  at expansion factor  $a_c$  is nonzero, infalling particles will not fall directly towards the halo center, but instead have a nonzero impact parameter, and the typical impact parameter determines the core size. Naively, we might expect that at formation ( $a = a_c$ ),

$$\frac{r_{\text{core}}}{r_{200}} \sim \frac{v_{\text{th}}}{v_{200}} \sim \left(\frac{\Omega_r}{\Omega_m} \frac{2}{\Delta_{200}^{1/3} a_c}\right)^{1/2} / \log\left(\frac{a_{\text{eq}}}{v_0}\right). \quad (3)$$

Following formation, any subsequent growth in halo mass can only decrease the core radius, while the virial radius can only increase. Indeed, even if the mass distribution around the halo is static, with no accretion following formation, the virial radius will still grow in time proportionally to the expansion factor  $a$ , because the expansion of the universe dilutes the background mean matter density. This is the reason why halo concentrations correlate with halo formation times in CDM cosmologies (e.g. Wechsler et al. 2002; Zhao et al. 2003a,b). Therefore, following the formation epoch  $a_c$ , the ratio  $r_{\text{core}}/r_{\text{vir}}$  must diminish in time at least as fast as  $a_c/a$ ; any mass accretion will only decrease this ratio even faster. Assuming no growth, then at the present time ( $a = 1$ )

$$\frac{r_{\text{core}}}{r_{200}} \sim \left(\frac{\Omega_r}{\Omega_m}\right)^{1/2} \left(\frac{2a_c}{\Delta_{200}^{1/3}}\right)^{1/2} / \log\left(\frac{a_{\text{eq}}}{v_0}\right). \quad (4)$$

This ratio is maximized by delaying halo formation as late as possible. For typical parameters, and setting  $a_c = 1$ , this gives  $r_{\text{core}} \approx 10^{-3} r_{200}$  observed today.

From this simple order-of-magnitude estimate, it appears unlikely that WDM models can produce sufficiently large core radii to explain LSB galaxies. This argument is only approximate, however. To make further progress, we have performed calculations of halo formation in WDM models. Our results indicate that WDM

halo cores are broadly consistent with (though typically smaller than) the above estimate, which precludes WDM as an explanation for the large cores that are claimed to exist in certain LSB galaxies.

## 2. NUMERICAL METHOD

In this section we describe our numerical method to solve for the self-consistent halo density profile following collapse. We eschew conventional N-body simulations, since for feasible simulation parameters the core radii will typically be unresolved or (at best) marginally resolved (Colín et al. 2008). Since we are interested in studying the behavior on scales smaller than the typical resolution limits of conventional N-body simulations, we have instead employed an alternative approach similar to that used by Lithwick & Dalal (2010).

We calculate the collapse of isolated peaks in an expanding universe. To isolate the effects of the nonzero WDM temperature during halo collapse, we focus on the case of spherical collapse. This problem has been investigated previously in the literature, and it is straightforward to show that cold, spherical collapse gives halos with central density profiles behaving as  $\rho \propto r^{-2}$ , or steeper (Fillmore & Goldreich 1984; Bertschinger 1985; Lithwick & Dalal 2010). Because cold spherical collapse is well-understood, any departures from  $r^{-2}$  profiles are clearly due to the effects of warm collapse. By Newton's theorem, our calculations neglect the effects of the local environment of peaks, which cause peaks to collapse nonspherically. We know from previous cosmological WDM simulations, however, that accounting for the effects of local environment does not lead to large cores in WDM halos (Colín et al. 2008; Wang & White 2009).

For a given potential  $\Phi(r, t)$ , assumed to be spherically symmetric, we integrate the equations of motion to solve for the orbit  $R(t)$  for each particle. Given the orbit  $R(t)$ , we compute the mass profile deposited by each particle. We compute orbits for many particles, and sum over all their deposited mass profiles to obtain the total mass profile  $M_{\text{total}}(r, t)$ , and the total density  $\rho = (dM_{\text{total}}/dr)/(4\pi r^2)$ . Then, we repeat this procedure, using the newly obtained mass profile, and iterate to convergence.

We initialize this procedure using linear perturbation theory. We start with a linear density profile  $\delta(r_L)$  describing the initial peak at the starting epoch  $a_{\text{init}} = (1 + z_{\text{init}})^{-1}$ . Here,  $r_L$  is a comoving Lagrangian radius, to be distinguished from the proper Eulerian radius  $r$  at subsequent times. We choose the initial peak profile to be proportional to the (linear theory) matter correlation function,  $\delta(r_L) \propto \xi(r_L)$ . This corresponds to the average profile of high peaks in the  $\nu \rightarrow \infty$  limit (Bardeen et al. 1986), and so this profile should be typical of the first halos to form in WDM cosmologies. The matter correlation function depends on the WDM transfer function, which Bode et al. (2001) found to be well described by the parametrization

$$T_{\text{WDM}}(k) = [1 + (\alpha k)^{2\nu}]^{-5/\nu}, \quad (5)$$

where  $\nu \approx 1.2$  and  $\alpha$  is a characteristic length scale. We parametrize WDM models by their free-streaming scale  $r_{\text{fs}}$ , or equivalently the enclosed mass  $M_{\text{fs}}$ , so we require a translation between  $r_{\text{fs}}$  and  $\alpha$ . We determine the equiv-

alent free-streaming length for a given  $\alpha$  by matching the Bode et al. transfer function to top-hat smoothing, which is given by

$$W_{\text{TH}}(k) = \frac{3}{(kR)^3} [\sin(kR) - kR \cos(kR)] \quad (6)$$

for smoothing scale  $R$ , which we take to be equal to  $r_{\text{fs}}$ . We have found that  $\alpha \approx 5r_{\text{fs}}$  provides a reasonable match to the two functions.

Given a desired free-streaming mass  $M_{\text{fs}}$  and halo formation redshift  $z_{\text{form}}$ , we set the initial peak profile shape  $\delta(r = a_{\text{init}} r_{\text{L}})$  to be proportional to the correlation function (using the appropriate  $r_{\text{fs}}$ ), and normalize the peak height at the starting redshift so that the average interior overdensity  $\bar{\delta} \equiv 3r^{-3} \int_0^r r'^2 \delta dr'$ , linearly evolved to redshift  $z_{\text{form}}$  and evaluated at the free-streaming scale is  $\bar{\delta}(r_{\text{L}} = r_{\text{fs}}, z = z_{\text{form}}) = \delta_c = 1.686$ , in accordance with the spherical collapse model (Gunn & Gott 1972). We assume that this linear profile evolves at early times according to linear perturbation theory:

$$\delta(r = a r_{\text{L}}, a) = D(a) \delta(r_{\text{L}}) \quad (7)$$

where  $D(a)$  is the linear growth factor, which for  $\Lambda$ CDM universes with no pressure perturbations may be expressed as

$$D(a) \propto H(a) \int_0^a \frac{da'}{(a'H)^3}, \quad (8)$$

normalized so that  $D(a = 1) = 1$  (Peebles 1980). Note that this procedure is not entirely self-consistent, since our use of CDM growth factors neglects the scale-dependence in WDM growth factors caused by residual free-streaming at late times. Our neglect of this residual free streaming when normalizing the initial peak height means that our peaks do not actually reach  $\delta = \delta_c$  at redshift  $z_{\text{form}}$ , leading to slight errors in the formation epoch. This does not appear to affect our results significantly.

This procedure specifies the initial overdensity perturbation at the starting redshift of the simulation. We also require the initial velocities for all the particles. These velocities have three contributions: the Hubble velocity, the bulk peculiar velocity, and a random thermal velocity. The Hubble term is of course just given by  $\mathbf{v}_H = H \mathbf{r}$ . The bulk peculiar velocity may be computed from the density profile, using the linearized continuity equation

$$\dot{\delta} + \nabla \cdot \mathbf{v} = 0, \quad (9)$$

along with the assumption of potential flow at early times (i.e.  $\nabla \times \mathbf{v} = 0$ ). This gives

$$v_r(r, a) \simeq -\frac{1}{3} r \dot{\delta}(r, a) H(a), \quad (10)$$

where again  $\bar{\delta} \equiv 3r^{-3} \int_0^r r'^2 \delta dr'$ . In addition to this bulk peculiar velocity, for each particle we add a thermal velocity, drawn from a Fermi-Dirac distribution function for WDM temperature  $T$ :

$$f(p, T) d^3p = \frac{1}{N_0(T)} \frac{p^2 dp}{e^{p/k_B T} + 1} \quad (11)$$

where the normalization is given by

$$N_0(T) = \int_0^\infty \frac{p^2 dp}{e^{p/T} + 1}. \quad (12)$$

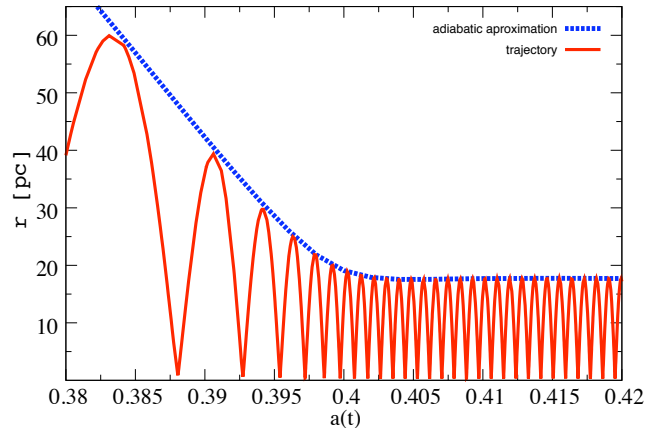


FIG. 1.— Adiabatic orbital evolution. The solid red curve shows an example orbit  $r(t)$  for a particle from one of our collapse calculations. For comparison, the dashed blue curve shows the expected behavior for the apoapse under the assumption that the orbit responds adiabatically to the deepening gravitational potential.

We typically begin at redshift  $z = 100$ . We sample 6000 initial radii spaced uniformly in volume, up to a maximum radius chosen to enclose the virialized region at  $z = 0$ . For each radius, we sample the momentum distribution with 500 points and the angular distribution with 200 points, weighting the particles according to the fraction of initial volume, solid angle, and momentum distribution that they represent.

Given the initial conditions for each particle, we then integrate forward the equations of motion using a fourth order, variable timestep Runge-Kutta integrator. The equations of motion are given by the usual Newtonian dynamics:

$$\frac{d^2 R}{dt^2} - \frac{L^2}{R^3} = -\nabla \Phi, \quad (13)$$

where the angular momentum  $\mathbf{L} = \mathbf{R} \times \mathbf{v}$  is conserved because of the assumed spherical symmetry.

Given an orbit  $R(t)$ , the enclosed mass profile deposited by each particle is

$$M(r, t) = m_p \Theta[r - R(t)], \quad (14)$$

where  $m_p$  is the mass represented by the particle, and  $\Theta(x)$  is the step function. Summing over all particles gives the total mass profile  $M_{\text{total}}(r, t)$ , and the density  $\rho(r, t)$  and potential  $\Phi(r, t)$  follow easily. Having computed the mass profile  $M(r, t)$  for a given iteration, we then use that mass profile in the equations of motion for the subsequent iteration. In practice, we bin the mass profile using a grid with 350 bins spaced uniformly in expansion factor  $a$  and 500 logarithmically spaced bins in radius, and then linearly interpolate from this grid to estimate the mass  $M$  at arbitrary times and radii as needed for the orbit integrations.

To expedite this calculation, we have made use of a simplifying approximation. For particles deep within the halo, whose orbital times are small compared to the Hubble time, we stop the orbital integration after the fractional change in the product  $R_{\text{apo}} \times M(R_{\text{apo}})$  over one orbit is less than  $10^{-3}$ . Thereafter, we assume that the orbit evolves adiabatically. Specifically, we assume that the radial action  $J_r = \oint v_r dR \propto [R_{\text{apo}} M(R_{\text{apo}})]^{1/2}$  is an adiabatic invariant. Given the time evolution of the mass

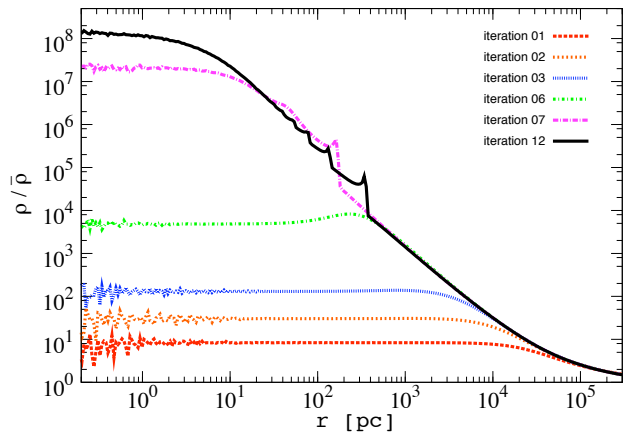


FIG. 2.— Convergence of the density profile. The halo density profile at  $z = 2.7$  after iterations 1,2,3,6 and 7 are shown in the colored curves, while the black curve shows the converged profile (12 iterations).

profile  $M(r, t)$ , we then easily determine the time evolution of the orbital apoapse  $R_{\text{apo}}$ . As Fig. 1 illustrates, adiabaticity is an excellent approximation for these orbits. Similarly, we assume that the ratio of periapse to apoapse,  $R_{\text{peri}}/R_{\text{apo}}$ , is also conserved because of conservation of angular momentum. Given  $R_{\text{peri}}$  and  $R_{\text{apo}}$ , we then assume that the mass profile deposited by this particle is

$$M(r, t) = m_p \times \begin{cases} 1, & \text{if } r > R_{\text{apo}} \\ \frac{r - R_{\text{peri}}}{R_{\text{apo}} - R_{\text{peri}}}, & \text{if } R_{\text{peri}} < r < R_{\text{apo}} \\ 0, & \text{if } r < R_{\text{peri}} \end{cases} \quad (15)$$

which is a good approximation to Eqn. (14), except for radii very near  $R_{\text{peri}}$  or  $R_{\text{apo}}$ .

This iterative procedure rapidly converges to a self-consistent collapse solution; Figure 2 illustrates one typical example. As the figure shows, the interior density profile quickly settles into roughly  $r^{-2}$  behavior, as expected, although there are features at both large radii and small radii. The spikes at large radii are caustics, a well-known feature of cold spherical collapse (Fillmore & Goldreich 1984; Vogelsberger et al. 2009). At small radii, discreteness effects of the finite number of particles leads to noise in the determined profile. This noise in the mass profile enters the equations of motion for particles, which affects particle orbits and leads to rapidly developing instabilities in the phase-space structure (Hénon 1973; Barnes et al. 1986; Henriksen & Widrow 1997). These instabilities significantly distort the shape of the radial caustics at times following collapse. We have checked that if we suppress these instabilities by artificially smoothing the potential, the caustics match the expected form. Because these instabilities are physical, rather than numerical in origin, we have opted not to suppress them. Accordingly, our density profiles at late times, long after collapse, do not show the expected prominent caustics.

### 3. RESULTS

In this section we present results of our calculations. In the first subsection, we illustrate the behavior found in one typical simulation, and in the following subsection

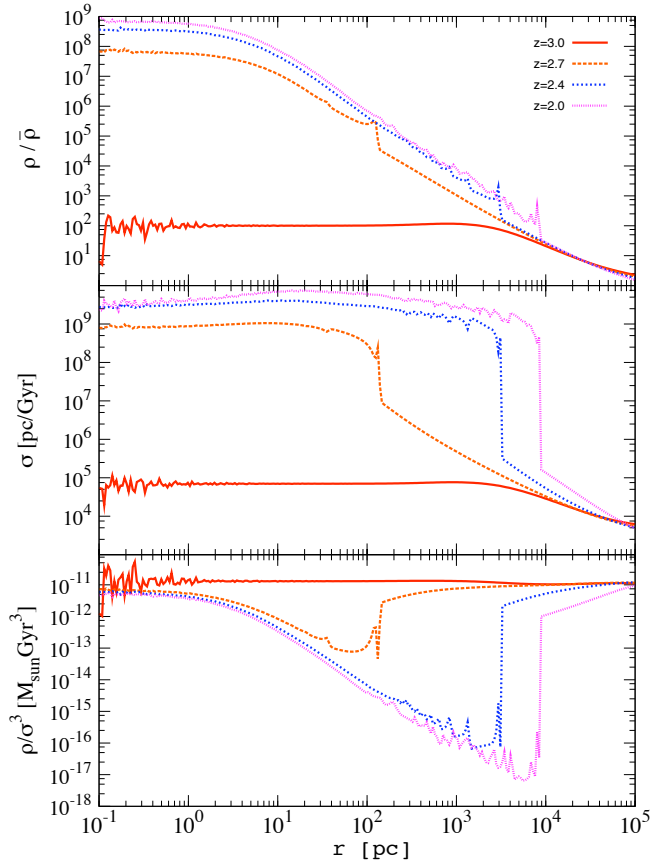


FIG. 3.— Collapsed profile as a function of time. The top panel shows the halo density profile  $\rho(r)$ , in units of the mean matter density  $\bar{\rho}$ , at various redshifts before, during, and after collapse at  $z \sim 2.7$ . The middle panel shows the 3-D velocity dispersion. The bottom panel shows the pseudo-phase-space density  $\rho/\sigma^3$ .

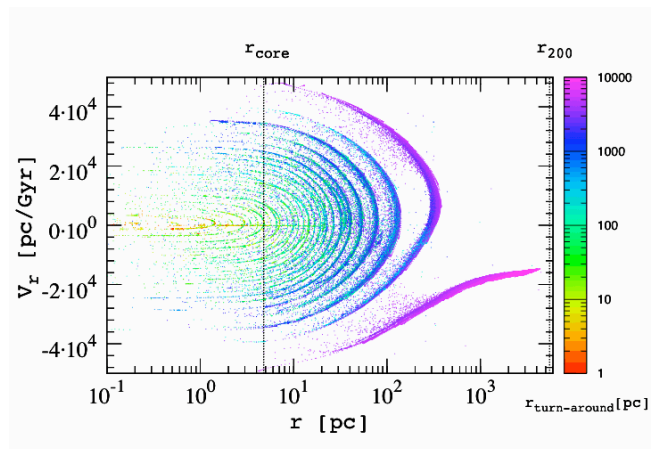


FIG. 4.— Radial behavior. Depicted are the radii  $r$  and radial velocities  $v_r$  for a subset of particles at  $z = 2.7$ . The color for each point indicates each particle’s turnaround radius. The vertical dotted lines indicate  $r_{\text{core}}$  and  $r_{200}$  at this redshift.

we describe how the behavior changes as we vary several physical parameters.

#### 3.1. Anatomy of a WDM halo

In this subsection, we describe the detailed results of one of our simulations. The behavior found for this halo

is representative of our simulations. For concreteness, we use a WDM temperature  $T_0/m = 1.3 \cdot 10^{-8}$  in units where  $c = 1$ , which gives a free-streaming scale  $r_{\text{fs}} \sim 100 h^{-1}$  kpc, and normalize the initial peak amplitude so that halo formation occurs near redshift  $z = 3$ . Figures 3 and 4 show the results. Figure 3 plots the density profile  $\rho(r)$ , the 3-D velocity dispersion  $\sigma(r)$ , and the pseudo-phase-space density  $\rho/\sigma^3$ , as a function of time, while Fig. 4 illustrates a snapshot in time of the radial dynamics. At early times, prior to collapse, the density evolves perturbatively, so that the  $\rho(r)$  profile is similar to the original linear density perturbation  $\delta(r)$ , simply growing in amplitude. The phase-space density remains very homogeneous before collapse. Near the time of collapse, there is smooth infall towards the halo, and both the density and velocity dispersion rise in concert to keep  $\rho/\sigma^3$  nearly constant. Orbits do cross in the infall region, however, since particles with different thermal velocities fall into the collapsing halo at different rates.

The initial collapse of the halo produces a roughly  $r^{-2}$  density profile, due to our assumption of spherical symmetry. This breaks to a shallower  $\rho \sim \text{const}$  behavior at the core radius  $r_{\text{core}}$ , where the infalling particles reach periapse. Following periapse, the particles splash back outwards with positive radial velocity. The splash-back surface defines the outermost caustic, where both the density and velocity dispersion jump precipitously. The density jumps at the caustic due to a pile-up of particles with similar apoapses. The velocity dispersion jumps because outside the caustic, particles are all falling inwards, whereas inside the caustic there is both outwards and inwards motion. Inside the caustic, the velocity dispersion remains roughly isothermal, at a value near the halo's virial velocity.

Because  $\rho \sim r^{-2}$  and  $\sigma$  is nearly constant with radius, the pseudo-phase space density shows a nearly power-law behavior over much of the virialized region. Outside the outermost caustic,  $\rho/\sigma^3$  remains nearly identical to the phase space density of the unperturbed material. At the caustic,  $\rho/\sigma^3$  falls steeply, due to the sudden increase in velocity dispersion. Towards smaller radii,  $\rho/\sigma^3$  rises smoothly, close to  $r^{-2}$ . It is important to stress, however, that  $\rho/\sigma^3$  is not a good proxy for the actual phase-space density over much of the halo's interior. The velocity dispersion tensor is highly anisotropic, in the sense that radial velocities are much larger than tangential velocities, as can be seen from the predominantly radial orbits shown in Figures 1 and 4. For this reason,  $\sigma \approx \sigma_r$ , and so  $\sigma^3 \approx \sigma_r^3 \gg \sigma_r \sigma_\theta \sigma_\phi$ . Only near the core radius does the velocity dispersion become close to isotropic.

Many of these features are similar to what is found in cold spherical collapse (Fillmore & Goldreich 1984; Bertschinger 1985). The most obvious difference between warm and cold collapse is the presence of a core radius, caused by the orbits' inability to reach  $r = 0$  due to their nonzero angular momenta. We estimate the core radius by fitting the density profile to the functional form

$$\rho = \frac{\rho_c}{\left[1 + \left(\frac{r}{r_{\text{core}}}\right)^\alpha\right]^{2/\alpha}}. \quad (16)$$

The parameter  $\alpha$  controls how sharply the profile breaks from  $r^{-2}$  behavior to constant density, and typically our

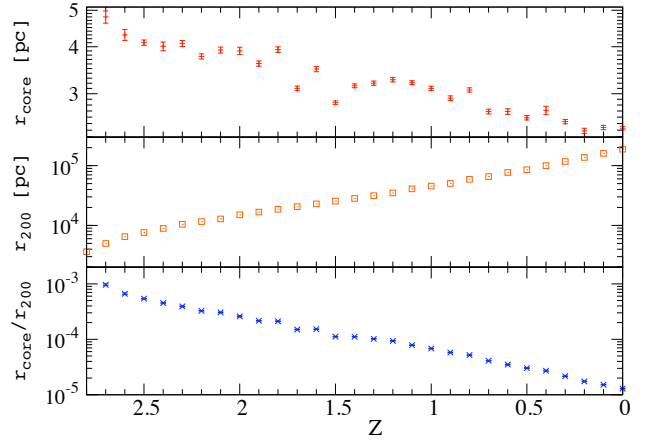


FIG. 5.— Time dependence of halo properties. The upper, middle and lower panels show  $r_{\text{core}}$ ,  $r_{200}$ , and the ratio  $r_{\text{core}}/r_{200}$  respectively, as a function of redshift. As the halo grows in mass over time, the virial radius grows, while the core radius shrinks due to adiabatic contraction. The ratio  $r_{\text{core}}/r_{200}$  is therefore maximized at the time of halo formation, and only diminishes thereafter.

simulations give  $\alpha \approx 1 - 2$ . We are mainly interested, however in the core radius. As Figure 4 shows,  $r_{\text{core}}$  coincides with the typical location of the periapse of the infalling particles. Both the density and pseudo-phase space density plateau at  $r_{\text{core}}$ , the latter saturating at a value near the phase space density of unvirialized material outside the halo as expected from the Tremaine & Gunn (1979) bound.

Figure 5 illustrates the evolution of the halo structural parameters over time. Following formation, the halo continues to accrete matter and steadily grows in mass, at a rate determined by the initial linear overdensity profile. By definition, this growth in  $M_{200}$  means that  $r_{200}$  grows as well. Note, however, that  $r_{\text{core}}$  decreases as the halo grows, due to adiabatic contraction of the orbits as the halo potential deepens over time. Since  $r_{\text{core}}$  only shrinks in time, while  $r_{200}$  grows in time, the ratio between the two is clearly maximized at the time of formation of the halo.

Lastly, in Figure 6 we plot the breakdown of the contributions to the mass profile from various radii. The left panel decomposes the particles into shells of initial radius at  $z = 100$ , while the middle panel uses bins of turnaround radius  $r_{\text{ta}}$ . At large radii,  $r \gg r_{\text{core}}$ , the mass is dominated by recently infalling particles that originated at large Lagrangian radius and have large turnaround radii, similar to the behavior found in cold spherical collapse (Fillmore & Goldreich 1984). However, this changes on scales of order the core radius. Near  $r_{\text{core}}$ , many different shells spanning decades in radius contribute comparably to the density. When we bin the particles based on initial, Lagrangian radius, we can see that each shell has a different core radius, roughly scaling as  $r_{\text{core}} \propto r_{\text{L}}$ , as may be expected from the arguments given in the introduction. When we bin the particles based on their turnaround radii, we can see that the typical apoapse for each shell scales like the turnaround radius. For shells with  $r_{\text{apo}} > r_{\text{core}}$ , the enclosed mass profile behaves as

$$M_{\text{shell}}(r) \propto r_{\text{L}}^3 \times \frac{r}{r_{\text{apo}}} \times \begin{cases} 1 & r \gg r_{\text{core}} \\ \left(\frac{r}{r_{\text{core}}}\right)^2 & r \ll r_{\text{core}} \end{cases} \quad (17)$$

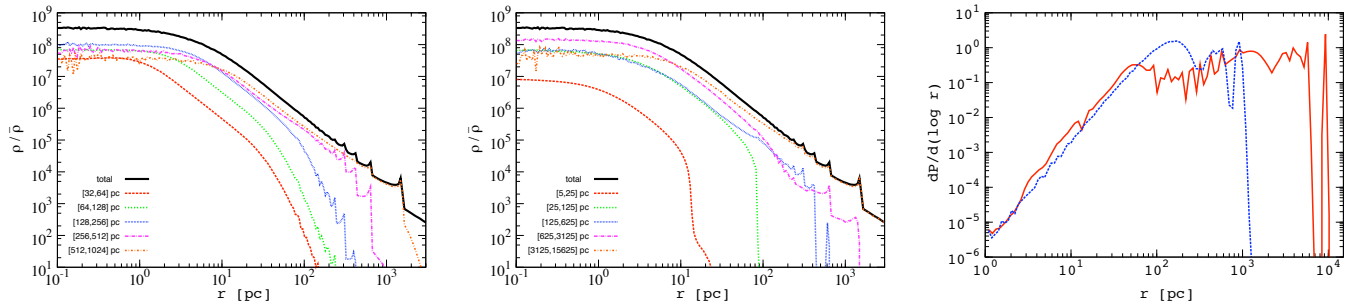


FIG. 6.— Breakdown of the mass distribution. The left panel shows the contribution to the mass density  $\rho(r)$  at  $z = 2.6$  originating from shells at various initial radii at  $z = 100$ . The middle panel shows a similar breakdown, instead binning particles based on their radii at turnaround. The right panel shows the distribution of initial radii (blue dashed) and turnaround radii (red solid) for all particles with  $r < r_{\text{core}}$  at  $z = 2.6$ .

and since  $r_{\text{core}} \propto r_L$  for each shell, we see that inside the core radius, the mass profile deposited by each shell of width  $d \log r_L$  scales as  $M_{\text{shell}} \propto r^3 \times (r_L/r_{\text{apo}}) \propto r^3 \times (r_L/r_{\text{ta}})$ . (For shells with  $r_{\text{apo}} < r_{\text{core}}$ , the enclosed mass simply behaves as  $M_{\text{shell}}(r) \propto (r_L r/r_{\text{core}})^3$ , of course.) For cold collapse, there is a one-to-one relationship between the turnaround radius  $r_{\text{ta}}$  and the initial radius, that depends on the initial linear density profile of the peak collapsing to form the halo. Roughly speaking, if locally the linear density has slope  $\gamma$ , in the sense that  $\delta \propto r_L^{-\gamma}$ , then  $r_{\text{ta}} \propto r_L^{1+\gamma}$  (Lithwick & Dalal 2010). The tight relationship between  $r_L$  and  $r_{\text{ta}}$  degrades somewhat for warm collapse, but we can still use the same basic scaling. For shells inside the free-streaming scale,  $r_L < r_{\text{fs}}$ , the peak profile is quite flat with local slope  $\gamma \approx 0$ , and so  $r_{\text{ta}} \propto r_L$ . For these shells,  $M_{\text{shell}}(r)$  becomes roughly independent of the shell’s initial radius for  $r < r_{\text{core}}$ , as is seen in Fig. 6. For larger radii,  $r_L \gtrsim r_{\text{fs}}$ , the slope of the initial profile becomes nonzero,  $\gamma > 0$ , implying that shells originating from large radii become subdominant inside the core radius. Thus, the mass inside the core radius is dominated by shells with  $r_L \lesssim r_{\text{fs}}$  and  $r_{\text{apo}} > r_{\text{core}}$ , and receives roughly equal contributions per decade within this range, as is seen in the right panel of Figure 6.

### 3.2. Dependence on physical parameters

Having established the basic features of the halo structure, we now explore the physics that sets those properties. The two main differences between WDM and CDM are the cutoff in the power spectrum, and the relic thermal velocities of DM particles at the time of halo formation. Both of these differences influence the size of halo core radii. To disentangle the different effects, we have performed collapse simulations in which we hold fixed the linear density profile of the initial peak, but vary the WDM temperature. This corresponds to holding fixed the halo assembly history, but varying the random motions near the time of collapse. The argument given in section 1 (e.g., Eqn. (3)) would predict that  $r_{\text{core}}$  would scale linearly with temperature, and our calculations appear consistent with this, as shown in Fig. 7. As we vary the temperature, the overall assembly history and structure of the halo remains unchanged (e.g., the location and height of the caustics), however the core radius varies. We find that a simple linear scaling,  $r_{\text{core}} \propto T$ , appears consistent with our simulations. We note, however, that this linear behavior breaks down at very high temper-

atures, when the particles’ random velocities become of order the Hubble velocity at the time of halo collapse. In this regime, the thermal motions are no longer a small perturbation to the particle dynamics, and the overall collapse of the halo is significantly modified, unsurprisingly. Of course, such calculations are not self-consistent: the large random motions that modify halo collapse at low redshift would have erased the initial linear density perturbations responsible for the halo, at a higher redshift.

This establishes that at fixed initial peak profile (i.e. fixed halo assembly history), the core radius scales linearly with DM temperature. It is inconsistent, however, to hold fixed the initial peak profile while the temperature is varied, since the random thermal motions of DM particles erase structure at high redshift and modify the peak profiles in the linear regime of structure formation. Therefore, we next explore how the core radius behaves as we self-consistently vary both the WDM temperature and the initial peak profile. We know that  $r_{\text{fs}}$  scales roughly linearly with  $T$ , and we have just seen that at fixed  $r_{\text{fs}}$ , the core radius  $r_{\text{core}}$  also scales linearly with  $T$ . Therefore, if  $r_{\text{core}}$  were independent of the halo assembly rate, then both  $r_{\text{core}}$  and  $r_{\text{fs}}$  would scale linearly with  $T$ , and the ratio  $r_{\text{core}}/r_{200}$  would be independent of the WDM temperature, as we argued in Section 1. Figure 8 shows that this behavior is not confirmed by our simulations, however. The figure shows the results of simulations using temperatures 5 times larger, and smaller, than our fiducial calculation. The red solid curve shows the density profile for  $r_{\text{fs}} = 20 h^{-1}$  kpc, orange dashed shows our fiducial run with  $r_{\text{fs}} = 100 h^{-1}$  kpc, and blue dotted shows results for  $r_{\text{fs}} = 500 h^{-1}$  kpc. In all three cases, we set the initial peak height so that collapse will occur near  $z = 3$ . As expected,  $r_{200}$  scales close to linearly with  $r_{\text{fs}}$ : the three simulations give  $r_{200} = 1.2, 5.5,$  and  $22.6$  kpc at the formation redshift  $z = 2.7$ . However,  $r_{\text{core}}$  does not scale linearly with  $r_{\text{fs}}$ : the three simulations give  $r_{\text{core}} = 0.6, 4.8$  and  $43$  pc respectively. The ratio  $r_{\text{core}}/r_{200}$  is not independent of  $r_{\text{fs}}$ , but instead behaves roughly as  $r_{\text{fs}}^{1/2}$  over the range that we have considered. Evidently, the core radius depends not only on the DM temperature at the time of halo formation, but also upon the halo assembly rate.

Lastly, we examine the dependence of the core radius on the halo formation time. We do so, simply by adjusting the height of the initial peak, holding fixed the WDM temperature and the radial shape of the peak pro-

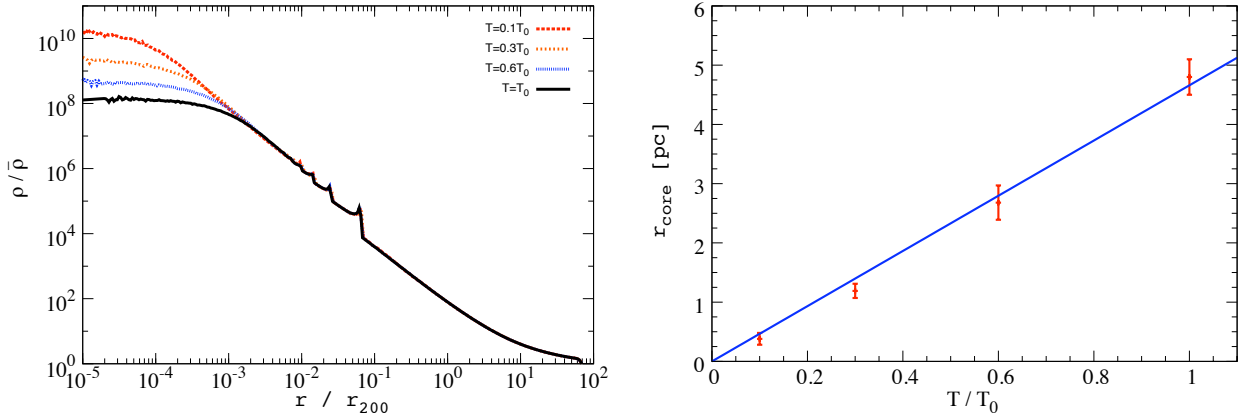


FIG. 7.— Temperature dependence of the halo profile for a fixed initial peak profile. (Left) The black solid curve shows the halo profile at redshift  $z = 2.7$  for  $T = T_0$ , where  $T_0$  is the WDM temperature consistent with the linear overdensity of the initial peak. For comparison, the red, orange and blue curves show the profile for  $T = 0.1T_0$ ,  $T = 0.3T_0$  and  $T = 0.6T_0$  respectively. (Right) The points show the fitted core radii for the profiles depicted in the left panel, using Eqn. (16), while the blue line shows a simple linear scaling  $r_{\text{core}} \propto T$ .

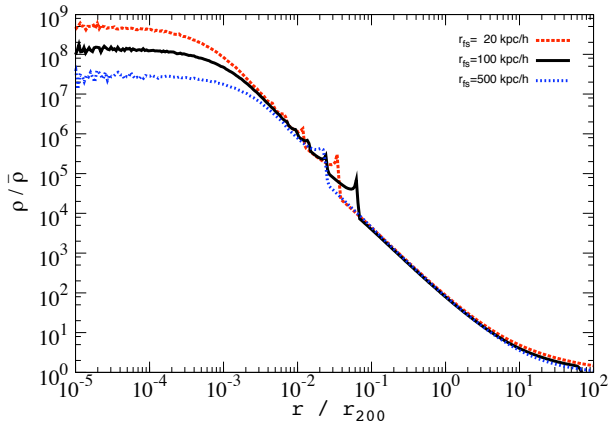


FIG. 8.— Effect of WDM temperature. Density profiles at  $z = 2.7$  for different initial peak profiles consistent with WDM temperature that produce  $r_{fs} = 20, 100$  and  $500$  kpc/h are plotted in dashed red, solid black and dotted blue lines respectively.

file. Figure 9 shows one example, comparing our fiducial simulation (with  $z_{\text{form}} = 2.7$ ) with a run using the same WDM temperature, but with initial peak height a factor of 4 larger. The later simulation has  $z_{\text{form}} = 13.6$ . The halo masses of the two simulations are similar, as expected:  $r_{200} = 1.3$  kpc for the  $z = 13.6$  halo, compared to  $r_{200} = 5.5$  kpc for the fiducial  $z = 2.7$  halo. The core radius for the earlier-forming halo is  $r_{\text{core}} = 2.8$  pc, compared to 4.8 pc for the fiducial halo, so that the ratio  $r_{\text{core}}/r_{200}$  changes by a factor of 2.8. The simple argument given in section 1 would have predicted that  $r_{\text{core}}/r_{200}$  would scale as  $(1 + z_{\text{form}})^{1/2}$ , whereas our simulation appears more consistent with a scaling  $r_{\text{core}}/r_{200} \propto (1 + z_{\text{form}})^{2/3}$ . This is only based on one comparison, of course. This is the result at the formation time; at  $z = 0$  the ratio  $r_{\text{core}}/r_{200}$  would be smaller by at least a factor of  $1/(1 + z_{\text{form}})$ , as we argued earlier.

#### 4. DISCUSSION AND SUMMARY

We have investigated the formation of halos in warm dark matter cosmologies. Our study of spherical collapse of WDM halos indicates that core radii do indeed arise in these cosmologies, as expected from simple phase-space arguments (Tremaine & Gunn 1979). However, we find that WDM core radii are generically small, typically of

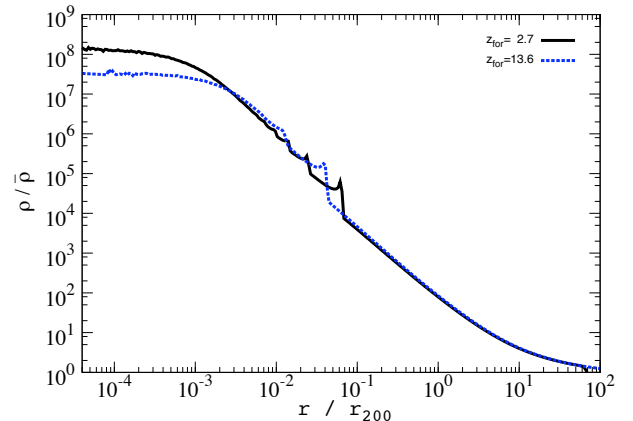


FIG. 9.— Effect of initial peak height. The solid black line shows the profile at collapse time  $z = 2.7$  for a peak height normalization of  $\delta(r_L = 100 h^{-1} \text{ kpc}, z = 3) = 1.686$ . In contrast, dashed blue shows the profile at collapse time  $z = 13.6$  for a peak height normalization of  $\delta(r_L = 100 h^{-1} \text{ kpc}, z = 15) = 1.686$ .

order  $10^{-3}$  of the halo virial radius at the time of formation, and considerably smaller following formation. This is for halos forming at the cutoff scale; higher mass halos will have substantially smaller  $r_{\text{core}}/r_{200}$ . We have investigated the dependence of the core radius on various physical parameters such as the WDM temperature, halo formation redshift, and halo mass. For the allowed range of WDM temperatures (e.g.  $M_{fs} \lesssim 10^9 M_{\odot}$ ), the core radii of halos observed at  $z = 0$  are generically expected to be far smaller than the core sizes measured in certain LSB galaxies, with  $r_{\text{core}}/r_{200} \approx 0.05$ .

Our calculations have all assumed spherical symmetry, whereas halo formation in both CDM and WDM cosmologies is highly nonspherical. We would argue, however, that our conclusions regarding WDM cores are likely to be valid for non-spherical collapse as well. One line of evidence supporting this argument is the fact that the pseudo-phase-space density profiles of our halos are quite similar to the profiles of halos in CDM simulations, with  $\rho/\sigma^3 \propto r^{-2}$ , roughly speaking (Ludlow et al. 2010). This similarity is presumably a consequence of the virial theorem, which ensures that  $\rho/\sigma^2 \sim r^{-2}$ . For WDM halos, the power-law rise of the pseudo-phase-space density towards small  $r$  saturates when  $\rho/\sigma^3$  approaches the

Tremaine-Gunn bound, and this saturation will occur for both spherical and nonspherical collapse. Now, we would expect the value of the pseudo-phase-space density to be similar at the virial radius for both spherical and non-spherical collapse, since the halo mass and virial radius are by definition the same in the two cases, and so  $\rho \sim M/4\pi r^3$  and  $\sigma \sim (GM_{200}/r_{200})^{1/2}$  will be similar for the two cases. We have noted that  $\rho/\sigma^3$  rises as roughly  $r^{-2}$  inside the virial radius in spherical and nonspherical collapse, and in both cases the core radius occurs where  $\rho/\sigma^3$  approaches the Tremaine-Gunn bound. So we have good reason to believe that halo core radii will not be significantly larger for nonspherical collapse than for spherical collapse, just because the  $\rho/\sigma^3$  profiles appear similar.

The other possible loophole in our argument is that we have assumed that no halos form below the cutoff scale in the power spectrum. N-body simulations have not

yet conclusively determined whether or not halos with  $M \ll M_{\text{fs}}$  arise in WDM cosmologies, due to numerical difficulties associated with simulating truncated power spectra (Wang & White 2007). We have begun investigating this issue, and our preliminary results indicate that halos may form below the cutoff scale, though it is unclear whether they can form in sufficient numbers to account for observed LSB galaxies.

Our results indicate that warm dark matter cosmologies cannot produce halos with core radii large enough to account for the density profiles of observed LSB galaxies. This would suggest that the origin of these observed cores lies within astrophysics, rather than particle physics.

We thank Manoj Kaplinghat, Mark Vogelsberger and Larry Widrow for useful discussions. FVN thanks CITA and the CFA for hospitality during the course of this work. ND is supported by CITA, and FVN is supported by CSIC pre-doctoral grant JAE 2008.

#### REFERENCES

- Bardeen, J. M., Bond, J. R., Kaiser, N., & Szalay, A. S. 1986, *ApJ*, 304, 15
- Barnes, J., Hut, P., & Goodman, J. 1986, *ApJ*, 300, 112
- Belokurov, V. et al. 2007, *ApJ*, 654, 897, arXiv:astro-ph/0608448
- Bertschinger, E. 1985, *ApJS*, 58, 39
- Bode, P., Ostriker, J. P., & Turok, N. 2001, *ApJ*, 556, 93, arXiv:astro-ph/0010389
- Colín, P., Valenzuela, O., & Avila-Reese, V. 2008, *ApJ*, 673, 203, arXiv:0709.4027
- Fillmore, J. A., & Goldreich, P. 1984, *ApJ*, 281, 1
- Governato, F. et al. 2009, ArXiv e-prints, arXiv:0911.2237
- Gunn, J. E., & Gott, III, J. R. 1972, *ApJ*, 176, 1
- Hénon, M. 1973, *A&A*, 24, 229
- Henriksen, R. N., & Widrow, L. M. 1997, *Physical Review Letters*, 78, 3426
- Kravtsov, A. 2010, *Advances in Astronomy*, 2010, 8, arXiv:0906.3295
- Kuzio de Naray, R., Martinez, G. D., Bullock, J. S., & Kaplinghat, M. 2010, *ApJ*, 710, L161, arXiv:0912.3518
- Lithwick, Y., & Dalal, N. 2010, in preparation
- Ludlow, A. D., Navarro, J. F., Springel, V., Vogelsberger, M., Wang, J., White, S. D. M., Jenkins, A., & Frenk, C. S. 2010, *MNRAS*, 406, 137, arXiv:1001.2310
- Navarro, J. F. et al. 2010, *MNRAS*, 402, 21, arXiv:0810.1522
- Peebles, P. J. E. 1980, *The large-scale structure of the universe* (Princeton University Press)
- Seljak, U., Makarov, A., McDonald, P., & Trac, H. 2006, *Physical Review Letters*, 97, 191303, arXiv:astro-ph/0602430
- Tollerud, E. J., Bullock, J. S., Strigari, L. E., & Willman, B. 2008, *ApJ*, 688, 277, arXiv:0806.4381
- Tremaine, S., & Gunn, J. E. 1979, *Physical Review Letters*, 42, 407
- Tremaine, S., Richstone, D. O., Byun, Y., Dressler, A., Faber, S. M., Grillmair, C., Kormendy, J., & Lauer, T. R. 1994, *AJ*, 107, 634, arXiv:astro-ph/9309044
- Vogelsberger, M., White, S. D. M., Mohayaee, R., & Springel, V. 2009, *MNRAS*, 400, 2174, arXiv:0906.4341
- Wang, J., & White, S. D. M. 2007, *MNRAS*, 380, 93, arXiv:astro-ph/0702575
- . 2009, *MNRAS*, 396, 709, arXiv:0809.1322
- Wechsler, R. H., Bullock, J. S., Primack, J. R., Kravtsov, A. V., & Dekel, A. 2002, *ApJ*, 568, 52, arXiv:astro-ph/0108151
- Zhao, D. H., Jing, Y. P., Mo, H. J., & Börner, G. 2003a, *ApJ*, 597, L9, arXiv:astro-ph/0309375
- Zhao, D. H., Mo, H. J., Jing, Y. P., & Börner, G. 2003b, *MNRAS*, 339, 12, arXiv:astro-ph/0204108